








Ultrafast laser inscribed waveguide lasers in Tm:CALGO with depressed-index cladding

VICTOR LLAMAS,^{1,2} PAVEL LOIKO,³ ESROM KIFLE,¹ CAROLINA ROMERO,⁴  JAVIER R. VÁZQUEZ DE ALDANA,⁴ ZHONGBEN PAN,^{5,6}  JOSEP MARIA SERRES,^{1,2}  HUALEI YUAN,⁵ XIAOJUN DAI,⁵ HUAQIANG CAI,⁵ YICHENG WANG,⁶  YONGGUANG ZHAO,^{6,7}  VIKTOR ZAKHAROV,⁸ ANDREY VENIAMINOV,⁸  ROMAIN THOUROUDE,² MATHIEU LAROCHE,² HERVÉ GILLES,² MAGDALENA AGUILÓ,¹ FRANCESC DÍAZ,¹ UWE GRIEBNER,⁶ VALENTIN PETROV,⁶ PATRICE CAMY,² AND XAVIER MATEOS^{1,*} 

¹ Física i Cristal·lografia de Materials i Nanomaterials (FiCMA-FiCNA)-EMaS, Dept. Química Física i Inorgànica, Universitat Rovira i Virgili (URV), Campus Sescelades, 43007 Tarragona, Spain

² Eurecat, Centre Tecnològic de Catalunya, Unitat Advanced Manufacturing Systems (AMS), Campus Sescelades, 43007 Tarragona, Spain

³ Centre de recherche sur les Ions, les Matériaux et la Photonique (CIMAP), UMR 6252

CEA-CNRS-ENSICAEN, Université de Caen, 6 Boulevard du Maréchal Juin, 14050 Caen Cedex 4, France

⁴ Aplicaciones del Láser y Fotónica, University of Salamanca, 37008 Salamanca, Spain

⁵ Institute of Chemical Materials, China Academy of Engineering Physics, 621900 Mianyang, China

⁶ Max Born Institute for Nonlinear Optics and Short Pulse Spectroscopy, Max-Born-Str. 2a, 12489 Berlin, Germany

⁷ Jiangsu Key Laboratory of Advanced Laser Materials and Devices, Jiangsu Normal University, 221116 Xuzhou, China

⁸ ITMO University, 49 Kronverkskiy Pr., 197101 St. Petersburg, Russia

*xavier.mateos@urv.cat

Abstract: Depressed-index buried and surface channel waveguides (type III) are produced in a bulk 3.5 at.% Tm³⁺:CALGO crystal by femtosecond direct-laser-writing at kHz repetition rate. The waveguides are characterized by confocal microscopy and μ -Raman spectroscopy. Under in-band-pumping at 1679 nm (³H₆ → ³F₄ transition) by a Raman fiber laser, the buried channel waveguide laser with a circular cladding (diameter: 60 μ m) generated a continuous-wave output power of 0.81 W at 1866–1947 nm with a slope efficiency of 71.2% (versus the absorbed pump power) and showed a laser threshold of 200 mW. The waveguide propagation losses were as low as 0.3 ± 0.2 dB/cm. The laser performance under in-band pumping was superior compared pumping at ~800 nm (³H₆ → ³H₄ transition), i.e., the conventional pump wavelength. Vibronic laser emission from the WG laser above 2 μ m is also achieved. The low-loss behavior, the broadband emission properties and good power scaling capabilities indicate the suitability of Tm³⁺:CALGO waveguides for mode-locked laser operation at ~2 μ m.

© 2020 Optical Society of America under the terms of the [OSA Open Access Publishing Agreement](#)

1. Introduction

Femtosecond (fs) Direct Laser Writing (DLW), also known as Ultrafast Laser Inscription (ULI) is a powerful method for the fabrication of passive and active photonic micro-structures such as optical waveguides (WGs) in transparent dielectric materials [1–3]. These materials absorb the energy of the fs pulses through nonlinear processes, leading to a permanent modification of the structure at the μ m-scale and, consequently, a change of the refractive index Δn with respect to the unmodified (bulk) regions [1]. The advantages of fs-DLW include the fast fabrication time, short interaction time preventing serious damage of the material, high precision, a wide range of

suitable materials (i.e., glasses, ceramics or crystals) and the ability to fabricate 3D structures as building blocks of photonic integrated circuits [4].

The classification of fs-DLW WGs is based on the refractive index change Δn which can be either positive or negative. In type I WGs (for $\Delta n > 0$), the mode guiding is observed *within* the irradiated area (typically, in the form of a damage track). Such conditions are common for amorphous materials such as glasses [5,6] and certain crystals [7]. In type II WGs (for $\Delta n < 0$), the guiding is achieved *between* a pair of damage tracks (the “dual-line” approach) or in the *vicinity* of a single track [8,9]. Within the irradiated areas, the refractive index decreases and between (near) the tracks, it is enhanced due to the photo-elastic effect. Compared to type I structures, type II WGs preserve their properties at increased temperature.

Recently, another geometry of depressed-index WGs was proposed [10] and classified as type III structures [1]. In type III WGs, the core is surrounded by a number of closely located damage tracks forming a quasi-continuous “wall” of reduced refractive index. The guided mode is then a bit separated from the WG cladding potentially reducing the propagation losses. Moreover, this approach allows one to control the transverse mode profile [11]. Typically, a circular geometry is more favorable as it fits the fiber technology.

WG lasers emitting in the eye-safe spectral range near $\sim 2 \mu\text{m}$ are of interest for optical communications, spectroscopy, sensing of relevant bio- and atmospheric molecules, and for further wavelength conversion to the mid-IR. It is common to achieve the $\sim 2 \mu\text{m}$ laser emission using thulium (Tm^{3+}) or holmium (Ho^{3+}) ions. Tm^{3+} ions typically feature large Stark splitting of the ground-state ($^3\text{H}_6$) leading to broadband luminescence and, thus, they are of interest for wavelength-tunable and ultrashort-pulse oscillators.

So far, efficient Tm WG lasers based on Liquid Phase Epitaxy (LPE) technology were demonstrated [12,13]. Van Dalfsen *et al.* reported on a $\text{Tm}:\text{KY}_x\text{Gd}_y\text{Lu}_z(\text{WO}_4)_2$ channel WG laser delivering up to 1.6 W at $1.84 \mu\text{m}$ with a slope efficiency of 75–81% employing a conventional pumping scheme (for the $^3\text{H}_6 \rightarrow ^3\text{H}_4$ transition, at $\sim 0.8 \mu\text{m}$) [12]. For Tm WG lasers fabricated by fs-DLW, typically, lower output powers were extracted [14–19]. Lancaster *et al.* demonstrated a fs-DLW channel WG laser in bulk $\text{Tm}:\text{ZBLAN}$ glass generating 205 mW at $1.89 \mu\text{m}$ and reaching a slope efficiency of 67% (using a similar pump) [15]. Note that for conventional pumping, to reach high slope efficiency, one needs to rely on the cross-relaxation for adjacent Tm^{3+} ions [12] leading to the requirement of high Tm^{3+} doping which might deteriorate the WG quality.

Further advances in the field of fs-DLW Tm WG lasers require (i) the search for novel materials supporting power-scalable laser operation and (ii) the introduction of an alternative pumping scheme which may intrinsically bring the advantage of high laser efficiency at any Tm^{3+} doping levels. Towards the first goal, in this work, we propose to use Tm^{3+} -doped calcium gadolinium aluminate (CaGdAlO_4 or shortly CALGO) crystal. This host material was first considered for Yb^{3+} doping [20] leading to high-power [21] and ultrashort-pulse mode-locked [22,23] lasers, including thin-disk lasers [24]. The key advantages of rare-earth doped CALGO are (i) good thermal properties, namely high thermal conductivity showing a weak dependence on the doping level [25] with weak and positive thermal lensing [26], and (ii) a structural disorder leading to inhomogeneous broadening of the spectral bands [27]. Channel WG lasers were fabricated in bulk $\text{Yb}^{3+}:\text{CALGO}$ by fs-DLW [28,29]. Hasse *et al.* reported on a WG laser based on the dual-line approach (type II) generating 2.4 W of output power at 1030–1042 nm with a slope efficiency of 69% (WG propagation losses of $\sim 1.1 \text{ dB/cm}$) [28].

Recently, the CALGO crystal and its yttrium isomorph (CALYO) were also implemented for Tm^{3+} doping. Hutchinson *et al.* first reported on spectroscopy of $\text{Tm}:\text{CALYO}$ crystals [30]. Laser operation was first achieved by Moncorge *et al.* [31]. Recent studies focused on diode-pumped laser performance and wavelength tuning [32]. Wang *et al.* demonstrated a SESAM mode-locked

Tm:CALGO bulk laser generating 650 fs pulses at 2021nm (emission bandwidth: ~ 9 nm) at a repetition rate of ~ 100 MHz [33].

The second goal is reached by implementing the so-called in-band or resonant pumping directly exciting the electrons to the upper laser level (3F_4). This concept has been already demonstrated for bulk Tm lasers. W. Yao *et al.* developed an in-band-pumped Tm³⁺:CALYO laser delivering 6.8 W at 1968 nm with a slope efficiency of $\sim 56\%$ [34]. Recently, it was implemented for Tm WG lasers based on the LPE fabrication technology: Loiko *et al.* achieved 2.05 W at 1881nm with a very high slope efficiency of 78.3% [35]. The advantages of in-band pumping are high slope efficiencies approaching the Stokes limit even at low Tm³⁺ doping levels and reduced heat loading.

In the present work, we demonstrate the first Tm³⁺:CALGO waveguide laser based on the fs-DLW fabrication method and implementing the in-band pumping scheme for reaching high slope efficiency and power scalability approaching the watt-level output.

2. Fabrication and characterization of waveguides

2.1. Femtosecond direct laser writing

As a gain material, we used bulk Tm:CALGO crystals grown by the conventional Czochralski method using Ar atmosphere in an Ir crucible and an [001]-oriented undoped seed [32]. Tm:CALGO is tetragonal (sp. gr. $I4/mmm - D_{4h}^{17}$). The crystal composition was determined by Inductively Coupled Plasma Mass Spectrometry as $\text{CaGd}_{0.913}\text{Lu}_{0.052}\text{Tm}_{0.035}\text{AlO}_4$. Optically passive Lu³⁺ ions were added to induce additional spectral broadening. The actual concentration of Tm³⁺ ions N_{Tm} was $4.31 \times 10^{20} \text{ cm}^{-3}$ (3.5 at.% Tm).

The laser crystal (thickness t : 6.2 mm, aperture: $3.2 \times 3.1 \text{ mm}^2$) was cut for light propagation along the crystallographic c -axis (c -cut), i.e. for σ -polarization. Both its input and output faces were polished to a laser-grade quality and left uncoated.

Depressed-index WGs were fabricated in bulk Tm:CALGO by fs-DLW. Two types of structures were produced, namely buried channel WGs with a circular cladding (diameter: 60, 80 and 100 μm), and surface channel WGs with a half-ring cladding (diameter: 60 μm). The WG cladding was formed by a set of continuous damage tracks produced in the crystal by fs laser radiation. Light guiding is expected in the core located within the cladding showing a decreased refractive index ($\Delta n = n_{\text{track}} - n_{\text{bulk}} < 0$), Fig. 1. Depressed cladding WGs are the only technique based on fs-laser irradiation that has been demonstrated to allow the fabrication of WGs for interaction with surface.

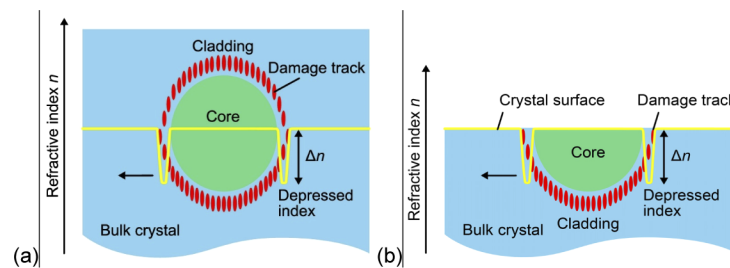


Fig. 1. Geometries of depressed-index (a) buried and (b) surface channel WGs (type III) fabricated in bulk Tm:CALGO crystal by fs-DLW.

For fs-DLW, we employed 120-fs, 795-nm pulses from a Ti:Sapphire regenerative amplifier operating at a repetition rate of 1 kHz [36]. The laser output was focused into the sample through the polished top surface using a $40\times$ microscope objective (N.A. = 0.65). Only a small fraction of the pulse energy was utilized and controlled with a $\lambda/2$ plate, a neutral density filter and a

polarizer. The writing parameters were optimized in a set of test experiments as follows: incident pulse energy of 0.25 μJ (buried WGs) and 0.17 μJ (surface one), writing speed of 400 $\mu\text{m/s}$ and track separation of 3 μm . To produce the damage tracks, the crystal was repetitively translated along its c -axis. The tracks were written along the entire length of the crystal. No post-writing repolishing of the crystal surfaces was applied as they were preserved undamaged.

2.2. Bulk crystal spectroscopy

Here, we briefly describe the spectroscopic properties relevant for laser operation. In the CALGO crystal, the Ca^{2+} and $\text{Gd}^{3+}|\text{Lu}^{3+}$ cations are statistically distributed over the same type of sites (C_{4v} symmetry, IX-fold oxygen coordination). The Tm^{3+} ions replace the Gd^{3+} cations. The local disorder originates from the second coordination sphere of Tm^{3+} [27]. Consequently, smooth and broad spectral bands both in absorption and emission are observed.

CALGO is an optically uniaxial crystal (the optical axis is parallel to the c -axis), so that there are two principal light polarizations, π and σ . At the wavelength of $\sim 1.92 \mu\text{m}$, its refractive indices are $n_o = 1.9021$ and $n_e = 1.9249$ [37].

The absorption cross-section spectra, σ_{abs} , for the transition from the $^3\text{H}_6$ ground-state to the excited-states of Tm^{3+} in CALGO, $^3\text{H}_4$ (conventional pumping) and $^3\text{F}_4$ (in-band pumping), are shown in Fig. 2(a) for π and σ polarizations. For the $^3\text{H}_6 \rightarrow ^3\text{H}_4$ transition, σ_{abs} is $0.67 \times 10^{-20} \text{ cm}^2$ at 798 nm and the full width at half maximum (FWHM) of the absorption band is 18.6 nm. For the $^3\text{H}_6 \rightarrow ^3\text{F}_4$ one, $\sigma_{\text{abs}} = 0.65 \times 10^{-20} \text{ cm}^2$ at 1736 nm with a larger FWHM of $\sim 120 \text{ nm}$ (all values are specified for σ -polarization).

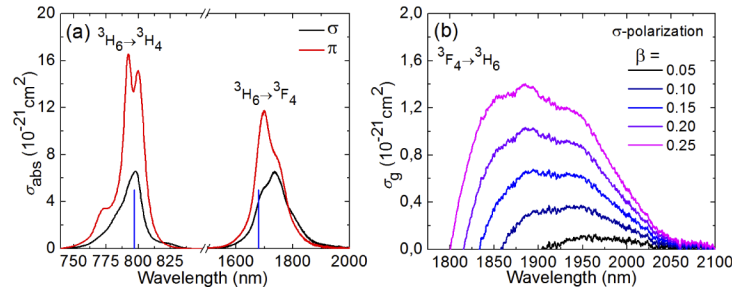


Fig. 2. Spectroscopy of Tm^{3+} ions in tetragonal CALGO crystals: (a) absorption cross-sections, σ_{abs} , for the $^3\text{H}_6 \rightarrow ^3\text{H}_4$ and $^3\text{H}_6 \rightarrow ^3\text{F}_4$ transitions (π and σ light polarizations), blue lines indicate the pump wavelengths in this work; (b) gain cross-sections, $\sigma_{\text{g}} = \beta\sigma_{\text{SE}} - (1 - \beta)\sigma_{\text{abs}}$, for σ -polarization, $\beta = N_2(^3\text{F}_4)/N_{\text{Tm}}$ is the inversion ratio for the $^3\text{F}_4 \rightarrow ^3\text{H}_6$ transition.

For the $^3\text{F}_4 \rightarrow ^3\text{H}_6$ laser transition, the maximum stimulated-emission (SE) cross-section σ_{SE} is $0.91 \times 10^{-20} \text{ cm}^2$ at 1813 nm for σ -polarization. Tm lasers operating on this transition represent a quasi-three-level laser scheme exhibiting reabsorption. To quantify this, the gain cross-sections for several inversion ratios are calculated in Fig. 2(b) for σ -polarization. The gain spectra of Tm:CALGO are smooth and broad. For an inversion ratio β of 0.20, the gain bandwidth is $\sim 145 \text{ nm}$. The upper laser level lifetime of Tm:CALGO is $\sim 3.2 \text{ ms}$.

2.3. Confocal microscopy

The geometry of the fabricated WGs was studied using a confocal laser microscope LSM 710 (Carl Zeiss). It was equipped with a rotatable polarizer (P), analyzer (A) and a blue GaN laser ($\lambda = 405 \text{ nm}$).

At first, we looked at one of the crystal end-facets in polarized light ($\text{P} \parallel \mathbf{a}$ -axis). The confocal microscope image for the buried WG with a circular cladding is shown in Fig. 3(a). One can

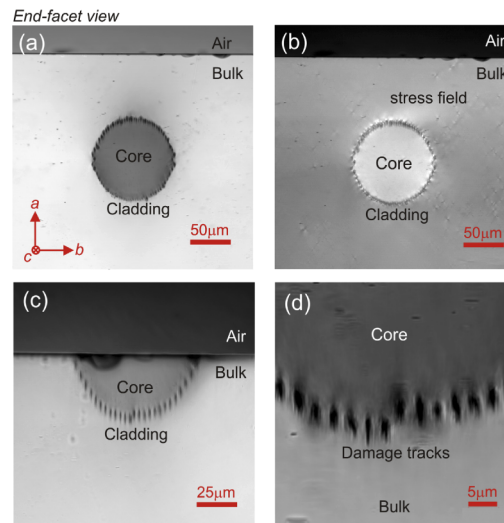


Fig. 3. WG end-face inspection: Confocal laser microscope images of depressed-index fs-DLW WGs in Tm:CALGO crystal: (a,b) buried WG with circular cladding (size: 100 μm); (c,d) surface WG with half-ring cladding (size: 60 μm). End-facet view, transmission mode, $\lambda = 405 \text{ nm}$, light polarization ($E \parallel a$) is vertical. Image (b) is obtained in crossed polarizers.

clearly see the WG cladding formed by individual damage tracks which appears darker than the surrounding bulk material, due to light scattering. The measured diameter of the cladding is $106 \times 104 \mu\text{m}$ (horizontal \times vertical) which is close to the targeted value ($\sim 100 \mu\text{m}$). The size of each individual damage track is $2 \times 6 \mu\text{m}$. This asymmetry is determined by the writing geometry (through the top surface). The separation between the tracks is $\sim 3 \mu\text{m}$ (horizontal) and $0\text{--}6 \mu\text{m}$ (vertical). The axis of the WG is located at $\sim 130 \mu\text{m}$ below the crystal surface. The area inside the cladding appears slightly darker (the greyscale colors are enhanced) possibly due to partial coupling of light into the WG and scattering at the cladding. There are no cracks originating from the fs-DLW.

By inspecting the same WG placed between two crossed polarizers ($P \parallel a$, $A \parallel b$), see Fig. 3(b), we observed a clear enhancement of the light intensity inside the WG cladding and around it. This is ascribed to the stress fields [38] caused by fs-DLW and inducing a local change of the optical indicatrix via the photo-elastic effect.

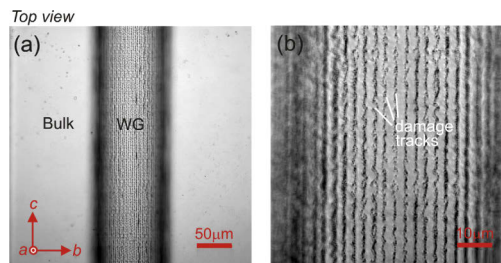


Fig. 4. WG top-surface inspection: Confocal laser microscope images of depressed-index fs-DLW WGs in Tm:CALGO crystal: (a,b) buried WG with a circular cladding (size: 100 μm). Top-view, transmission mode, $\lambda = 405 \text{ nm}$, light polarization ($E \parallel c$) is vertical.

A similar study is performed for the surface WG, Fig. 3(c). The measured size of this WG is $72 \times 40 \mu\text{m}$ (horizontal \times vertical). The WG is located just beneath the crystal surface: the distance to the most shallow damage tracks is only $6 \mu\text{m}$. The cracks in Fig. 3(c) originate from polishing of the WG end-facet before the fabrication of the WG. Figure 3(d) gives a close look on individual damage tracks.

Subsequently, we examined the top surface of the sample in polarized light ($P \parallel c$). The canvas-like barrel-shape cladding of the buried WGs is clearly seen in Fig. 4(a). No cracks are observed in the surrounding bulk region. By observing the individual damage tracks, Fig. 4(b), we conclude that they are continuous along the writing direction. The width of the tracks is $\sim 1 \mu\text{m}$ and the deviation from a straight line is less than $2 \mu\text{m}$.

2.4. μ -Raman spectroscopy

Raman spectroscopy is sensitive to weak modifications of the structure of the host material. For μ -Raman studies, we used a Renishaw inVia Reflex confocal Raman microscope equipped with a $50\times$ Leica objective and an Ar^+ ion laser ($\lambda = 514 \text{ nm}$).

The Raman spectrum of the c -cut Tm:CALGO crystal is shown in Fig. 5. The maximum phonon energy is $\sim 650 \text{ cm}^{-1}$.

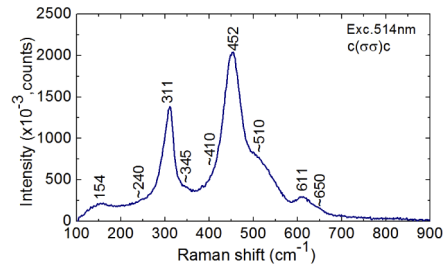


Fig. 5. Raman spectrum of the c -cut Tm:CALGO bulk crystal. The measurement geometry is $c(\sigma\sigma)c$, $\lambda_{\text{exc}} = 514 \text{ nm}$. The numbers indicate the Raman frequencies in cm^{-1} .

For μ -Raman mapping of the crystal end-facet, we selected the vibration at $\sim 452 \text{ cm}^{-1}$ and monitored this Raman peak intensity, width and position. The results for the buried WG with a circular cladding (diameter: $100 \mu\text{m}$) are shown in Fig. 6. In the area containing the damage tracks, the Raman peak intensity decreases, the peak is broadened and a shift of its position is observed. These changes indicate modification of the material in the irradiated area, in particular, a reduction of its crystallinity [39]. In Figs. 6(b) and 6(c), one can also see a slight variation of the Raman response in the areas outside the cladding which are spatially matching the stress fields

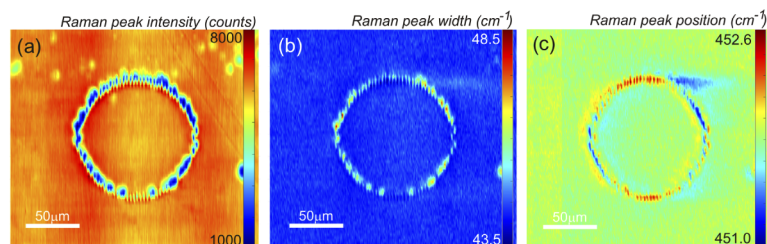


Fig. 6. μ -Raman mapping of a depressed-index buried channel WG with a circular cladding (size: $100 \mu\text{m}$) fabricated in a Tm:CALGO crystal by fs-DLW: (a) peak intensity, (b) width (FWHM), (c) position; monitoring the $\sim 452 \text{ cm}^{-1}$ mode in the $c(\sigma\sigma)c$ geometry, $\lambda_{\text{exc}} = 514 \text{ nm}$.

suggested by the confocal microscopy study, Fig. 3(b). In the WG core, the Raman response of the material is very close to that in the bulk crystal, confirming no alteration of the crystal structure in the core.

3. Laser operation

3.1. Laser set-up

The scheme of the in-band pumped WG laser is shown in Fig. 7(a). The crystal containing the WGs was mounted on a passively-cooled Cu-holder using a silver paste for better heat removal. The laser cavity was formed by a flat pump mirror (PM) coated for high transmission (HT, $T = 93.0\%$) at $1.68 \mu\text{m}$ and for high reflection (HR) at $1.86\text{--}2.32 \mu\text{m}$, and a set of flat output couplers (OCs) with transmissions T_{OC} of 1.5% – 50% at the laser wavelength. We also used a band-pass OC supporting laser oscillation above $2 \mu\text{m}$. Both the PM and the OC were placed as close as possible to the crystal. No index-matching liquid was used to avoid damage to the optical elements.

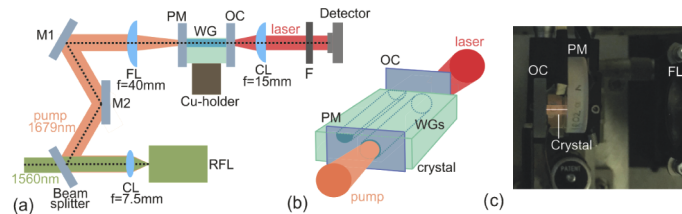


Fig. 7. Scheme of the in-band-pumped Tm:CALGO WG laser: (a) laser set-up, CL and FL – collimating and focusing lens, respectively, M1 and M2 – folding mirrors, PM – pump mirror, OC – output coupler, WG – waveguide, F – cut-on filter, RFL – Raman fiber laser; (b) geometry of the studied WG lasers (buried and surface); (c) photograph of the laser.

As a pump source for in-band pumping (${}^3\text{H}_6 \rightarrow {}^3\text{F}_4$ transition), we used a home-made Raman fiber laser (RFL) delivering up to 2.9 W of linearly polarized output at 1679 nm ($M^2 \approx 1$, emission bandwidth: $< 1 \text{ nm}$) [40]. The fundamental beam was provided by an erbium fiber master oscillator power amplifier (MOPA) configuration. The RFL was based on a single-mode polarization maintaining germanosilicate fiber (iXBlue Photonics; core diameter, $4.5 \mu\text{m}$; length, 300 m) exhibiting a Raman-active mode with energy of $\sim 440 \text{ cm}^{-1}$. The output of the RFL was collimated with a lens (focal length: $f = 7.5 \text{ mm}$), filtered from the residual pump at 1560 nm using a beam-splitter and focused into the crystal through the PM with an uncoated spherical CaF_2 lens ($f = 40 \text{ mm}$).

The measured pump spot diameter in the focus $2w_p$ was $30 \pm 5 \mu\text{m}$. The pump coupling efficiency η_{coupl} was estimated from the Fresnel losses at the uncoated input crystal facet to be 90.3% ($n_o = 1.9055$ [37]). The single-pass pump absorption was calculated from the small-signal value, $\eta_{\text{abs},0(1\text{-pass})} = 1 - \exp(-\sigma_{\text{abs}}^p N_{\text{Tm}} t) = 64.5\%$ ($\sigma_{\text{abs}}^p = 0.40 \times 10^{-20} \text{ cm}^2$ is the absorption cross-section at the pump wavelength λ_p for σ -polarization).

The geometry of the buried and channel WG lasers is shown in Fig. 7(b). A photograph of this laser is presented in Fig. 7(c).

The laser emission after the OC was collimated using a spherical CaF_2 lens ($f = 15 \text{ mm}$) and filtered from the residual pump using a dichroic mirror. The spectra of laser emission were measured using an optical spectrum analyzer (model AQ6375B, Yokogawa). The beam profile was captured using a FIND-R-SCOPE near-IR camera.

A similar set-up was used for pumping at $\sim 800 \text{ nm}$ (${}^3\text{H}_6 \rightarrow {}^3\text{H}_4$ transition), e.g., the conventional pump wavelength. For this, we employed a Ti:Sapphire laser (model Mira 900, Coherent) emitting up to 1.5 W at $\lambda_p = 798 \text{ nm}$ ($M^2 \approx 1$). The pump light was collimated using a microscope

objective (Mitutoyo M Plan NIR 10 \times , N.A. = 0.28, $f = 20$ mm, $T = 63.8\%$ at 0.80 μm) resulting in $2w_p = 20 \pm 5$ μm . The flat PM was coated for HT ($T > 99\%$) at 0.80 μm and for HR at 1.8 – 2.1 μm and the set of flat OCs had a transmission T_{OC} of 1.5% – 30% at the laser wavelength. The residual pump was filtered with a long-pass filter (FEL1000, Thorlabs).

The pump coupling efficiency was estimated from the pump-transmission measurements at ~ 850 nm (outside the Tm^{3+} absorption band), e.g., for the buried WG with a circular cladding (size: 60 μm), $\eta_{\text{coupl}} = 81 \pm 2\%$ (accounting for the Fresnel losses). The pump absorption at the threshold pump power was determined from similar measurements at 798 nm, $\eta_{\text{abs,L}(1\text{-pass})} = 83 \pm 2\%$, being close to the small-signal one.

The near-field profiles of the pump modes for the conventional ($\lambda_p = 798$ nm) and in-band ($\lambda_p = 1679$ nm) pumping are shown in Fig. 8. For $\lambda_p = 798$ nm, the pump radiation almost uniformly fills the volume of the WG core. At the wavelength of $\lambda_p = 1679$ nm, less modes are supported. Still, they are well confined within the WG cladding (shown by red circles).

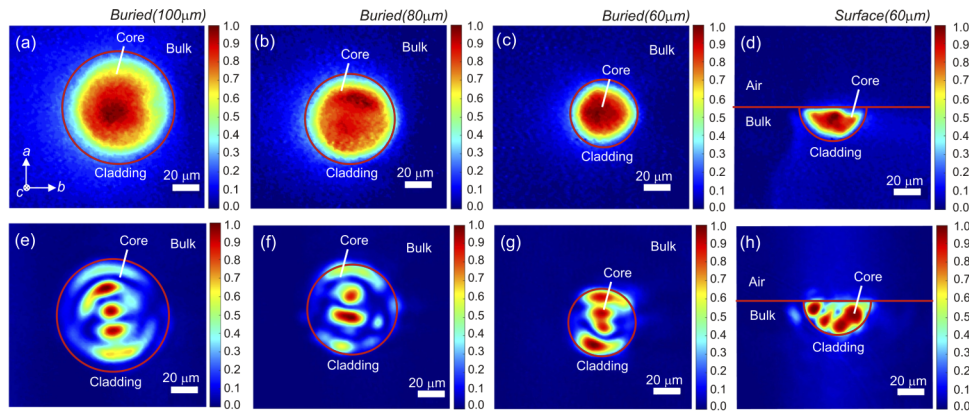


Fig. 8. Near-field pump modes for depressed-index fs-DLW channel WGs in $\text{Tm}:\text{CALGO}$: (a)-(c) $\lambda_p = 798$ nm, (e)-(f) $\lambda_p = 1679$ nm; buried WGs with a circular cladding and a diameter of (a,e) 100 μm , (b,f) 80 μm , (c,g) 60 μm and (d,h) surface WG with a half-ring cladding (size: 60 μm). The red circular lines indicate the cladding / crystal surface and are drawn as a guide for the reader.

3.2. WG laser pumped at 798 nm - conventional pumping

We started the laser experiments using the conventional pumping ($\lambda_p = 798$ nm). The input-output dependences for the buried channel WG (diameter: 60 μm) are presented in Fig. 9(a). The WG laser generated a maximum output power of 0.27 W at 1824 – 1832 nm with a slope efficiency η of 50.3% (vs. the absorbed pump power P_{abs}) and a laser threshold of $P_{\text{th}} = 92$ mW. The optical-to-optical efficiency η_{opt} was 29.6% (vs. the incident power on the crystal). The highest output power corresponded to $T_{\text{OC}} = 30\%$ (the maximum available output coupling in this experiment). We did not observe any thermal roll-over in the output dependences, damage of the WG end-facets or fracture of the WG itself. For lower output coupling, the slope efficiency gradually decreased.

The determined value of the slope efficiency exceeds the limit set by the Stokes efficiency, $\eta_{\text{St}} = \lambda_p / \lambda_L = 43.6\%$ (λ_L is the laser wavelength), which indicates the effect of cross-relaxation between adjacent Tm^{3+} ions.

Typical laser emission spectra are shown in Fig. 9(b). For $T_{\text{OC}} < 30\%$, the emission occurred in several spectral regions, at 1.85 , 1.88 , 1.90 and 1.93 μm . For example, for the lowest studied $T_{\text{OC}} = 1.5\%$, it was at 1851 – 1936 nm. This spectral behavior is attributed to the broad gain spectra

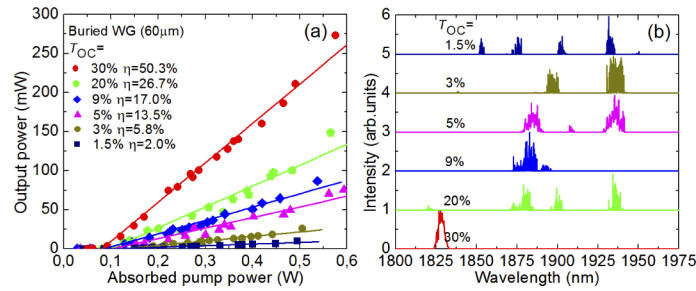


Fig. 9. Fs-DLW Tm:CALGO channel waveguide laser pumped at $\lambda_P = 798$ nm (conventional pumping): (a) input-output dependences, η – slope efficiency; (b) laser emission spectra measured at $P_{\text{abs}} = 0.4$ W. Buried WG with a circular cladding (diameter: $60 \mu\text{m}$).

of Tm:CALGO, cf. Figure 2(b). For $T_{\text{OC}} = 30\%$, the emission wavelength was shorter, around $1.83 \mu\text{m}$. The laser emission was unpolarized in all cases.

Typical modes of laser emission in the near-field for all four studied WGs are shown in Fig. 10. The laser modes are clearly different from the pump ones, Figs. 8(a)–8(d). This is because less transverse modes are supported for the same Δn at longer wavelengths and because of mode competition. In all cases, the laser mode was well confined within the WG cladding.

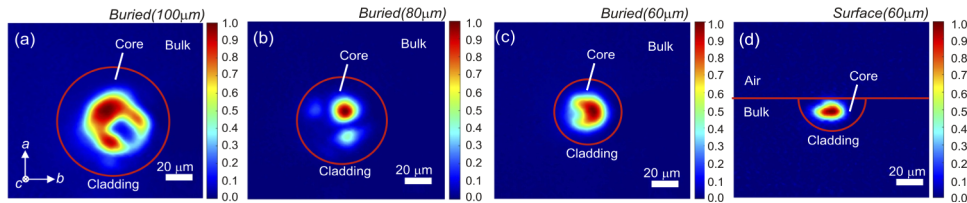


Fig. 10. Near-field spatial profiles of the laser mode for Tm:CALGO WG lasers using conventional pumping ($\lambda_P = 798$ nm): (a)–(c) buried WGs with a circular cladding (diameter: (a) $100 \mu\text{m}$, (b) $80 \mu\text{m}$, (c) $60 \mu\text{m}$); (d) surface WG with a half-ring cladding (size: $60 \mu\text{m}$). The red circular lines indicate the cladding / crystal surface and are drawn as a guide for the reader. $T_{\text{OC}} = 20\%$.

3.3. WG laser pumped at 1679 nm - in-band pumping

The performance of the buried channel WG laser (size: $60 \mu\text{m}$) for different output coupling is shown in Fig. 11(a). The WG laser generated a maximum output power of 0.81 W at 1866 – 1947 nm with a slope efficiency η of 71.2% and showed a laser threshold P_{th} of 200 mW. The optical-to-optical laser efficiency η_{opt} amounted to 35.8% . These results were achieved for the optimum T_{OC} of 30% . For higher output coupling, the efficiency slightly deteriorated due to the upconversion losses related to high population inversion. The unpolarized laser emission was broadband, Fig. 11(b), similar as in the case of pumping at 798 nm [Fig. 9(b)] due to the flat and broad gain spectra. The spectral behavior was also determined by the etalon (Fabry-Perot) effects at the crystal / mirror interfaces.

The performance of the in-band pumped WG laser is superior compared to the conventional pumping both in terms of the output power and slope efficiency.

The comparison of the laser performance of all four studied WGs is shown in Fig. 11(c) for the same $T_{\text{OC}} = 20\%$. For the buried WGs, the output power increased slightly with the WG diameter, reaching 0.88 W at 1907 – 1938 nm with $\eta = 69.7\%$ and $P_{\text{th}} = 70$ mW for the WG with the largest cross-section ($100 \mu\text{m}$). The performance of the surface WG was inferior which is

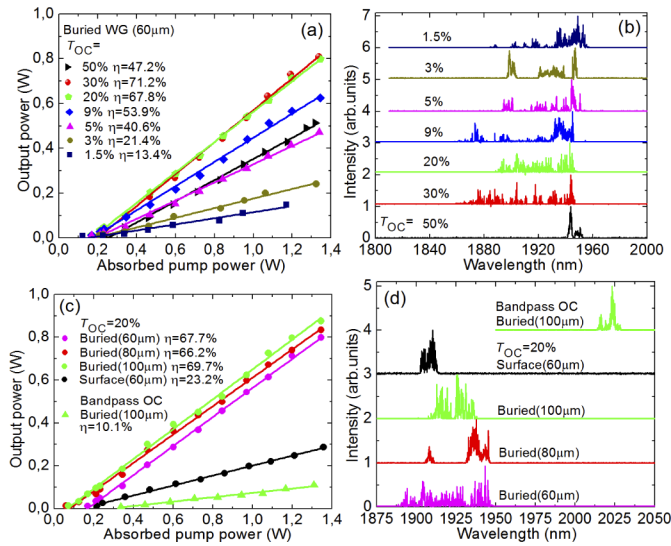


Fig. 11. Fs-DLW Tm:CALGO channel waveguide lasers in-band pumped at 1679 nm: (a,b) buried WG with a circular cladding (size: 60 μm), (c,d) comparison of buried (size: 60–100 μm) and surface (size: 60 μm) WGs, $T_{OC} = 20\%$, (a,c) input-output dependences, η – slope efficiency; (b,d) typical laser emission spectra measured at $P_{abs} = 1.5$ W.

attributed to higher propagation losses: the surface WG laser generated 0.29 W at 1902–1913nm with lower η of 23.2% and increased P_{th} of 210 mW. The laser emission spectra of different WG lasers are shown in Fig. 11(d) and they are similar.

The WG propagation losses estimated from the Caird analysis [41] were $\sim 0.3 \pm 0.2$ dB/cm (for the buried channel WG with a diameter of 60 μm), Fig. 12. This value is comparable to that estimated for fs-DLW depressed-index WGs in bulk Tm^{3+} :ZBLAN glass (0.4 ± 0.2 dB/cm) [15]. Compared to the previously reported type II WGs in Yb^{3+} :CALGO [28], we measured much lower propagation losses.

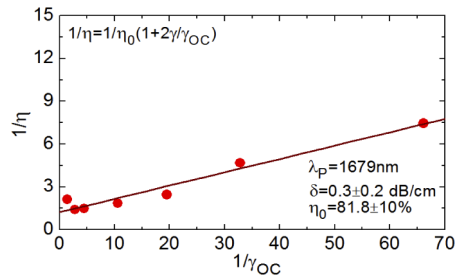


Fig. 12. Caird analysis of intracavity losses in the in-band pumped Tm:CALGO buried WG laser (circular cladding with a diameter of 60 μm): inverse of the slope efficiency, $1/\eta$, vs. inverse of the output-coupling loss, $1/\gamma_{OC}$, circles – experimental data, line - their fit.

By implementing the band-pass OC, we achieved laser emission above 2 μm: the buried channel WG laser (diameter: 100 μm) generated up to 0.11 W at 2015–2028nm. However, lasing at such long wavelengths was at the expense of a reduced slope efficiency ($\eta = 10.1\%$) and an increased laser threshold ($P_{th} = 335$ mW). Let us analyze this operation regime. The Stark splitting for Tm^{3+} ions in CALGO is unknown. For the isostructural Tm:CALYO crystal [30], the longest wavelength of a purely electronic transition $^3F_4 \rightarrow ^3H_6$ is 1959nm as it occurs between

the sub-levels with energies of 5689 and 584 cm^{-1} . The emission at longer wavelengths can be however observed due to the electron-phonon coupling (vibronic emission) [42]. In particular, the broad low-energy phonon mode at $\sim 154 \text{ cm}^{-1}$, cf. Figure 4, may participate in this process.

Typical laser emission modes for the in-band pumped WG lasers are shown in Fig. 13. The laser modes were well confined within the WG cladding. For all buried WGs, the emission was spatially multimode. For the surface WG, the mode was close to the fundamental transverse one maybe due to the smaller WG volume and stronger mode competition under higher losses.

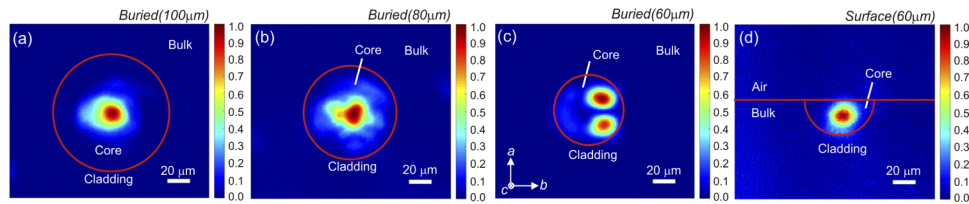


Fig. 13. Near-field profiles of the laser mode for in-band pumped Tm:CALGO WG lasers: (a)-(c) buried WGs with a circular cladding (diameter: (a) 100 μm , (b) 80 μm , (c) 60 μm); (d) surface WG with a half-ring cladding (size: 60 μm). The red circular lines indicate the cladding / crystal surface and are drawn as a guide for the reader. $T_{\text{OC}} = 20\%$.

For in-band pumping, the upper limit for the laser slope efficiency can be estimated from the Stokes one, $\eta_{\text{St}} \approx 87\%$. The achieved slope efficiency, Fig. 11(a), is close to this value. The main physical reasons for the reduced η are (i) non-perfect overlap of the pump and laser modes (a single transverse mode WG with a smaller diameter of the cladding is required to optimize the mode overlap) and (ii) possible upconversion losses in Tm³⁺:CALGO associated with high inversion ratios β (populations of the upper laser level, 3F_4) which are expected to be suppressed with the optimization of the Tm³⁺ doping level.

4. Conclusion

The first $\sim 2 \mu\text{m}$ waveguide lasers based on the CALGO crystalline host have been demonstrated. We have confirmed, Tm³⁺:CALGO is a suitable crystalline material for efficient and power-scalable 2- μm waveguide lasers due to its high thermal conductivity, good thermo-mechanical properties, and broad and smooth Tm³⁺ emission bands originating from the structural disorder. Employing fs direct laser writing, we have fabricated low-loss depressed-index buried and surface channel waveguides with a circular and half-ring cladding (classified as type III). Confocal laser microscopy and μ -Raman spectroscopy confirmed the well-preserved single-crystalline nature of the material in the WG core region, its modification in the cladding and suggested the role of the stress fields in additional variation of the refractive index. The Tm:CALGO waveguide lasers feature high CW output power (approaching the watt-level), high laser slope efficiency of more than 70% and extremely broadband emission properties (free-running emission: 1866-1947nm, vibronic emission: 2015–2028nm). The excellent output performance was achieved employing the in-band pumping scheme.

The proposed scheme of in-band pumping using Raman fiber lasers paves the way towards multi-watt output from fs direct laser written Tm waveguide lasers. Indeed, in the present paper, we were mostly limited by the available power from the fiber laser which could be increased to $>10 \text{ W}$. We expect that the optimization of the Tm³⁺ doping level and the WG length will allow for a simultaneous control of upconversion losses and pump absorption. Regarding the material, it is also promising to study *a*-cut crystals giving access to π -polarization showing higher absorption cross-sections and linearly polarized laser output. In the present work, we selected *c*-cut crystals because of the crystal growth direction.

Fs direct laser written Tm³⁺:CALGO waveguides with a smaller cladding diameters (30–50 μm) are expected to support a single transverse mode which, together with low propagation losses and broadband emission, makes them promising for compact mode-locked oscillators operating at high (GHz-range) repetition rates.

Funding

Ministerio de Economía y Competitividad (FIS2017-87970-R, MAT2016-75716-C2-1-R (AEI/FEDER,UE)); Consejería de Educación, Junta de Castilla y León (SA287P18); Agència de Gestió d'Ajuts Universitaris i de Recerca (2017SGR755); Agence Nationale de la Recherche (LabEx EMC3 project FAST-MIR); European Commission (FEDER); Generalitat de Catalunya (2016FI_B00844, 2017FI_B100158, 2018FI_B200123).

Acknowledgments

This work was supported by the Normandie region.

Disclosures

The authors declare no conflicts of interest.

References

1. F. Chen and J. R. Vázquez de Aldana, "Optical waveguides in crystalline dielectric materials produced by femtosecond-laser micromachining," *Laser Photonics Rev.* **8**(2), 251–275 (2014).
2. R. R. Gattass and E. Mazur, "Femtosecond laser micromachining in transparent materials," *Nat. Photonics* **2**(4), 219–225 (2008).
3. S. Nolte, M. Will, J. Burghoff, and A. Tuennermann, "Femtosecond waveguide writing: a new avenue to three-dimensional integrated optics," *Appl. Phys. A* **77**(1), 109–111 (2003).
4. G. D. Marshall, A. Politi, J. C. F. Matthews, P. Dekker, M. Ams, M. J. Withford, and J. L. O'Brien, "Laser written waveguide photonic quantum circuits," *Opt. Express* **17**(15), 12546–12554 (2009).
5. K. M. Davis, K. Miura, N. Sugimoto, and K. Hirao, "Writing waveguides in glass with a femtosecond laser," *Opt. Lett.* **21**(21), 1729–1731 (1996).
6. A. M. Streltsov and N. F. Borrelli, "Study of femtosecond-laser-written waveguides in glasses," *J. Opt. Soc. Am. B* **19**(10), 2496–2504 (2002).
7. A. Rodenas and A. K. Kar, "High-contrast step-index waveguides in borate nonlinear laser crystals by 3D laser writing," *Opt. Express* **19**(18), 17820–17833 (2011).
8. J. Siebenmorgen, T. Calmano, K. Petermann, and G. Huber, "Highly efficient Yb:YAG channel waveguide laser written with a femtosecond-laser," *Opt. Express* **18**(15), 16035–16041 (2010).
9. G. A. Torchia, A. Rodenas, A. Benayas, E. Cantelar, L. Roso, and D. Jaque, "Highly efficient laser action in femtosecond-written Nd:yttrium aluminum garnet ceramic waveguides," *Appl. Phys. Lett.* **92**(11), 111103 (2008).
10. A. G. Okhrimchuk, A. V. Shestakov, I. Khrushchev, and J. Mitchell, "Depressed cladding, buried waveguide laser formed in a YAG:Nd³⁺ crystal by femtosecond laser writing," *Opt. Lett.* **30**(17), 2248–2250 (2005).
11. H. Liu, Y. Jia, J. R. V. de Aldana, D. Jaque, and F. Chen, "Femtosecond laser inscribed cladding waveguides in Nd:YAG ceramics: Fabrication, fluorescence imaging and laser performance," *Opt. Express* **20**(17), 18620–18629 (2012).
12. K. van Dalen, S. Aravazhi, C. Grivas, S. M. García-Blanco, and M. Pollnau, "Thulium channel waveguide laser with 1.6 W of output power and ~80% slope efficiency," *Opt. Lett.* **39**(15), 4380–4383 (2014).
13. P. Loiko, R. Souillard, G. Brasse, J.-L. Doualan, B. Guichardaz, A. Braud, A. Tyazhev, A. Hideur, and P. Camy, "Watt-level Tm:LiYF₄ channel waveguide laser produced by diamond saw dicing," *Opt. Express* **26**(19), 24653–24662 (2018).
14. D. G. Lancaster, S. Gross, H. Eboroff-Heidepriem, K. Kuan, T. M. Monro, M. Ams, A. Fuerbach, and M. J. Withford, "Fifty percent internal slope efficiency femtosecond direct-written Tm³⁺:ZBLAN waveguide laser," *Opt. Lett.* **36**(9), 1587–1589 (2011).
15. D. G. Lancaster, S. Gross, A. Fuerbach, H. E. Heidepriem, T. M. Monro, and M. J. Withford, "Versatile large-mode-area femtosecond laser-written Tm:ZBLAN glass chip lasers," *Opt. Express* **20**(25), 27503–27509 (2012).
16. Y. Ren, G. Brown, A. Ródenas, S. Beecher, F. Chen, and A. K. Kar, "Mid-infrared waveguide lasers in rare-earth-doped YAG," *Opt. Lett.* **37**(16), 3339–3341 (2012).
17. J. Morris, N. K. Stevenson, H. T. Bookey, A. K. Kar, C. T. A. Brown, J.-M. Hopkins, M. D. Dawson, and A. A. Lagatsky, "1.9 μm waveguide laser fabricated by ultrafast laser inscription in Tm:Lu₂O₃ ceramic," *Opt. Express* **25**(13), 14910–14917 (2017).

18. E. Kifle, P. Loiko, J. R. V. de Aldana, C. Romero, A. Ródenas, S. Y. Choi, J. E. Bae, F. Rotermund, V. Zakharov, A. Veniaminov, M. Aguiló, F. Díaz, U. Griebner, V. Petrov, and X. Mateos, "Passively Q-switched femtosecond-laser-written thulium waveguide laser based on evanescent field interaction with carbon nanotubes," *Photonics Res.* **6**(10), 971–980 (2018).
19. E. Kifle, P. Loiko, X. Mateos, J. R. V. de Aldana, A. Ródenas, U. Griebner, V. Petrov, M. Aguiló, and F. Díaz, "Femtosecond-laser-written hexagonal cladding waveguide in Tm:KLu(WO₄)₂: μ -Raman study and laser operation," *Opt. Mater. Express* **7**(12), 4258–4268 (2017).
20. J. Petit, P. Goldner, and B. Viana, "Laser emission with low quantum defect in Yb:CaGdAlO₄," *Opt. Lett.* **30**(11), 1345–1347 (2005).
21. P. Loiko, J. M. Serres, X. Mateos, X. Xu, J. Xu, V. Jambunathan, P. Navratil, A. Lucianetti, T. Mocek, X. Zhang, U. Griebner, V. Petrov, M. Aguiló, F. Díaz, and A. Major, "Microchip Yb:CaLnAlO₄ lasers with up to 91% slope efficiency," *Opt. Lett.* **42**(13), 2431–2434 (2017).
22. Y. Zauouter, J. Didierjean, F. Balembois, G. Lucas Leclin, F. Druon, P. Georges, J. Petit, P. Goldner, and B. Viana, "47-fs diode-pumped Yb³⁺:CaGdAlO₄ laser," *Opt. Lett.* **31**(1), 119–121 (2006).
23. P. Sévillano, P. Georges, F. Druon, D. Descamps, and E. Cormier, "32-fs Kerr-lens mode-locked Yb:CaGdAlO₄ oscillator optically pumped by a bright fiber laser," *Opt. Lett.* **39**(20), 6001–6004 (2014).
24. N. Modsching, C. Paradis, F. Labaye, M. Gaponenko, I. J. Graumann, A. Diebold, F. Emaury, V. J. Wittwer, and T. Südmeyer, "Kerr lens mode-locked Yb:CALGO thin-disk laser," *Opt. Lett.* **43**(4), 879–882 (2018).
25. P. Loiko, F. Druon, P. Georges, B. Viana, and K. Yumashev, "Thermo-optic characterization of Yb:CaGdAlO₄ laser crystal," *Opt. Mater. Express* **4**(11), 2241–2249 (2014).
26. F. Druon, M. Olivier, A. Jaffrès, P. Loiseau, N. Aubry, J. Didierjean, F. Balembois, B. Viana, and P. Georges, "Magic mode switching in Yb:CaGdAlO₄ laser under high pump power," *Opt. Lett.* **38**(20), 4138–4141 (2013).
27. P. O. Petit, J. Petit, P. Goldner, and B. Viana, "Inhomogeneous broadening of optical transitions in Yb:CaYAlO₄," *Opt. Mater.* **30**(7), 1093–1097 (2008).
28. K. Hasse, T. Calmano, B. Deppe, C. Liebald, and C. Kränkel, "Efficient Yb³⁺:CaGdAlO₄ bulk and femtosecond-laser-written waveguide lasers," *Opt. Lett.* **40**(15), 3552–3555 (2015).
29. K. Hasse and C. Kränkel, "Yb:CALGO waveguide laser written with 1 MHz-repetition rate fs-laser," in *Laser Congress 2019 (ASSL, LAC, LS&C)*, OSA Technical Digest (Optical Society of America, 2019), P. ATu1A.7.
30. J. A. Hutchinson, H. R. Verdun, B. H. Chai, B. Zandi, and L. D. Merkle, "Spectroscopic evaluation of CaYAlO₄ doped with trivalent Er, Tm, Yb and Ho for eyesafe laser applications," *Opt. Mater.* **3**(4), 287–306 (1994).
31. R. Moncorgé, N. Garnier, P. Kerbrat, C. Wyon, and C. Borel, "Spectroscopic investigation and two-micron laser performance of Tm³⁺:CaYAlO₄ single crystals," *Opt. Commun.* **141**(1-2), 29–34 (1997).
32. Z. Pan, P. Loiko, J. M. Serres, E. Kifle, H. Yuan, X. Dai, H. Cai, Y. Wang, Y. Zhao, M. Aguiló, F. Díaz, U. Griebner, V. Petrov, and X. Mateos, "Mixed" Tm:Ca(Gd,Lu)AlO₄ - a novel crystal for tunable and mode-locked 2 μ m lasers," *Opt. Express* **27**(7), 9987–9995 (2019).
33. Y. Wang, G. Xie, X. Xu, J. Di, Z. Qin, S. Suomalainen, M. Guina, A. Härkönen, A. Agnesi, U. Griebner, X. Mateos, P. Loiko, and V. Petrov, "SESAM mode-locked Tm:CALGO laser at 2 μ m," *Opt. Mater. Express* **6**(1), 131–136 (2016).
34. W. Yao, F. Wu, Y. Zhao, H. Chen, X. Xu, and D. Shen, "Highly efficient Tm:CaYAlO₄ laser in-band pumped by a Raman fiber laser at 1.7 μ m," *Appl. Opt.* **55**(14), 3730–3733 (2016).
35. P. Loiko, R. Thouroude, R. Soulard, L. Guillemot, G. Brasse, B. Guichardaz, A. Braud, A. Hideur, M. Laroche, H. Gilles, and P. Camy, "In-band pumping of Tm:LiYF₄ channel waveguide: a power scaling strategy for ~2 μ m waveguide lasers," *Opt. Lett.* **44**(12), 3010–3013 (2019).
36. E. Kifle, X. Mateos, J. R. V. de Aldana, A. Ródenas, P. Loiko, S. Y. Choi, F. Rotermund, U. Griebner, V. Petrov, M. Aguiló, and F. Díaz, "Femtosecond-laser-written Tm:KLu(WO₄)₂ waveguide lasers," *Opt. Lett.* **42**(6), 1169–1172 (2017).
37. P. Loiko, P. Becker, L. Bohatý, C. Liebald, M. Peltz, S. Vernay, D. Rytz, J. M. Serres, X. Mateos, Y. Wang, X. Xu, J. Xu, A. Major, A. Baranov, U. Griebner, and V. Petrov, "Sellmeier equations, group velocity dispersion, and thermo-optic dispersion formulas for CaLnAlO₄ (Ln = Y, Gd) laser host crystals," *Opt. Lett.* **42**(12), 2275–2278 (2017).
38. H.-D. Nguyen, A. Ródenas, J. R. Vázquez de Aldana, J. Martínez, F. Chen, M. Aguiló, M. C. Pujol, and F. Díaz, "Heuristic modelling of laser written mid-infrared LiNbO₃ stressed-cladding waveguides," *Opt. Express* **24**(7), 7777–7791 (2016).
39. E. Kifle, P. Loiko, C. Romero, J. R. V. de Aldana, A. Ródenas, V. Zakharov, A. Veniaminov, M. Aguiló, F. Díaz, U. Griebner, V. Petrov, and X. Mateos, "Femtosecond-laser-written Ho:KGd(WO₄)₂ waveguide laser at 2.1 μ m," *Opt. Lett.* **44**(7), 1738–1741 (2019).
40. R. Thouroude, H. Gilles, B. Cadier, T. Robin, A. Hideur, A. Tyazhev, R. Soulard, P. Camy, J. L. Doualan, and M. Laroche, "Linearly-polarized high-power Raman fiber lasers near 1670 nm," *Laser Phys. Lett.* **16**(2), 025102 (2019).
41. J. A. Caird, S. A. Payne, P. R. Staber, A. J. Ramponi, L. L. Chase, and W. F. Krupke, "Quantum electronic properties of the Na₃Ga₂Li₃F₁₂:Cr³⁺ laser," *IEEE J. Quantum Electron.* **24**(6), 1077–1099 (1988).
42. P. Loiko, X. Mateos, S. Y. Choi, F. Rotermund, J. M. Serres, M. Aguiló, F. Díaz, K. Yumashev, U. Griebner, and V. Petrov, "Vibronic thulium laser at 2131 nm Q-switched by single-walled carbon nanotubes," *J. Opt. Soc. Am. B* **33**(11), D19–D27 (2016).